Coupling CFD-DEM with dynamic meshing: A new approach for fluid-structure interaction in particle-fluid flows

Yi. He *, Andrew E. Bayly, Ali Hassanpour

School of Chemical and Process Engineering, University of Leeds, Leeds, LS2 9JT, UK

ABSTRACT

Many important engineering applications involve the interaction of free-moving objects with dispersed multi-phase flows, however due to the challenge and complexity of modelling these systems, modelling approaches remain very limited and very few studies have been reported. This work presents a new method capable of addressing these problems. It integrates a dynamic meshing approach, used to explicitly capture the flow induced by free-moving large object(s), with a conventional CFD-DEM method to capture the behaviour of small particles in particle-fluid flow. The force and torque acting on the large object due to the fluid flow are explicitly calculated by integrating pressure and viscous stress acting on the object's surface and the forces due to collisions with both the smaller particles and other structures are calculated using a soft-sphere DEM approach. The developed model has been fully implemented on the ANSYS/Fluent platform due to its efficient handling of dynamic meshing and complex and/or free-moving boundaries, thus it can be applied to a wide range of industrial applications. Validation tests have been carried out for two typical gas-solid fluidization cases, they show good qualitative and quantitative agreement with reported experimental literature data. The developed model was then successfully applied to gas fluidization with a large immersed tube which was either fixed or free-moving. The predicted interacting dynamics of the gas, particle and tube were highly complex and highlighted the value of fully resolving the flow around the large object. The results demonstrated that the capability of a conventional CFD-DEM approach could be enhanced to address free-body fluid-structure interaction problems encountered in particle-fluid systems.

1. Introduction

The interaction between large objects and particle-fluid flows is commonly encountered in a wide range of applications such as fluidization [1], chemical reactors [2–5], mineral processing, milling [6,7] and drug delivery devices [8]. The objects can have different forms, such as fixed/free-moving internal structures or large free particles, whose size is at least one order of magnitude larger than the small particles that make up the majority of particles present. The co-existence of a large object can have an important impact on the behaviour of the particulate phase, such as mixing, segregation, heat and mass transfer rate [9]. For example, in gas-fluidized beds, immersed tubes are often used to effectively remove heat from the system and to avoid hot spots caused by chemical reaction [10,11]. In coal and wooden biomass combustion processes, large fuel particles can affect mixing and segregation behaviour [2,3]. In some intensified chemical reactors, a free moving agitator is used for mixing and particle suspension [4,5]. In the general case of a free object, its motion is determined by both the fluid flow and its interaction with other particles, and conversely, the flow field and particle behaviour are affected by the movable object. Thus, successful modelling of the dynamics of such a multi-scale system requires a method to solve fluid-structure interaction (FSI) problems in particle-fluid flows.

Numerical models of particle-fluid flows can be largely classified into three methods according to the treatment of the particulate and the fluid phases: Eulerian-Eulerian methods, Lagrangian-Lagrangian methods and Eulerian-Lagrangian methods [12–14]. In Eulerian-Eulerian methods, both the fluid and particulate phase are described as interpenetrating continuous phases [15,16]. Constitutive or closure relations are required to describe the solid phase pressure and viscosity. Despite its advantages in handling large-scale industrial systems as a continuum approach, these models lack the capability to access information at the particle scale due to pseudo-fluid assumption of the particulate phase. More recently, the application of Lagrangian-Lagrangian methods, such as SPH-SPH [17] and SPH-DEM coupling [18,19], has gained popularity due to their capability in handling free-surface flows, large deformations and deformable boundaries but at a cost of high computational time. As a compromise, Eulerian-Lagrangian methods, which are normally referred as coupled CFD-DEM approaches when particle-particle collisions are resolved, are widely used. In coupled CFD-DEM, the particles are tracked individually using Newton's second law of motion while the fluid flow is determined

by CFD methods on a computational cell level. The forces acting on particles are explicitly considered, thus a quantitative description of the particle behaviour can be obtained. To date, most CFD-DEM studies are concerned with fixed geometries, such as immersed tubes in fluidized systems. Different approaches have been used to treat the stationary boundary of the tube in CFD calculation either using staircase approximation on a Cartesian grid [20,21] or accurately representing the boundary shape using body-fitted unstructured mesh [22,23]. Considerable efforts have been devoted to various aspects of the fluidized bed, including heat transfer [21,24,25], bubble hydrodynamics [20,26] and erosion of the tube surface [27]. However, the capability of CFD-DEM methods to tackle FSI problems in particle-fluid flow is lacking, especially when the fluid field is described by a continuous mesh-based method, such as Finite Volume Method (FVM) or Finite Difference Method (FDM). In these cases where the free-object is represented by a single or cluster of DEM elements, the computational mesh is normally required to be larger than the dimensions of the object or the size of the largest particle present in the system to avoid the mesh being fully occupied by the solid phase. Therefore, the applicability of the conventional CFD-DEM approach is limited to particles with small size ratio. Recently, Alobaid et al. [28] introduced an additional grid for the particulate phase. The grid resolution is allowed to be smaller than the particle size. More accurate predictions of the particle motion and pressure drop are reported for the fluidized bed [28,29]. However, phase interaction in these methods is still modelled by drag correlations, which inevitably leads to a lack of detailed flow structure around the large object. Therefore, developing a new model to overcome the limitations of the conventional CFD-DEM approach in addressing FSI problem encountered in particle-fluid flow is of great importance to both research and industrial practice.

Due to the presence of large free-moving object, a resolved method is necessary to obtain the induced fluid structure. Several improvements have been proposed under the CFD-DEM framework which are potentially applicable to the FSI problem in particle-fluid flow. The immersed boundary method (IBM) allows the use of a rectangular grid for complex geometries [30] and has been applied to dispersed multiphase flow. Takeuchi et al. [31] applied it to treat the cone surface of spouted beds, with no dynamic motion of the boundaries. Guo et al. [32] introduced the IBM to a CFD-DEM model and applied to several systems with moving boundaries including a study of segregation in a vertically vibrated bed, however, no systems with free-body motion were reported. The only work on free-body motion in these multi-phase systems is reported by Tsuji et al. [33] who represent the large object using small fictitious spheres using an idea similar to the volume penalization method. The solidity of immersed object is approximated by means of permeability controlled by input parameters of fictitious particle diameter and solid volume fraction inside the object. Although the flow at the bodies boundary is not fully resolved, experimental validation showed good agreements on the position of a free-moving large sphere during and after stopping the fluidization [33,34]. Its applicability for more complex geometries is not clear, and additional computational costs will be required for complex geometries in order to identify those computational cells containing the solid structure. Moreover, it is worth noting that the above models may face challenges in the resolution of boundary layers in turbulent flows.

With increasing demand on engineering applications, coupling DEM with versatile commercial or open source CFD software, for instance, Fluent, CFX, OpenFOAM and MFIX, among many others, is gaining popularity due to its generality and capability in handling complex geometrical boundaries and robust turbulence handling. To implement the coupling, two sets of model formulations are commonly used, referred as Model A and B, depending on the treatment of pressure in the governing .equations [35]. Pressure is attributed to the fluid phase alone in the model B while it is shared by both the fluid and solid phases in the model A. To date, most of the coupling is based on the formulation of model A. Based on the model A, Wu et al. [36] coupled a hard sphere

model with Fluent based on its single phase model through rearrangement of the governing equation. Special treatment is needed to ensure mass conservation [37]. Liu et al. [23] coupled DEM with Fluent based on the Eulerian multiphase model in Fluent. A similar strategy is also adopted in coupling between commercial software, like Fluent-EDEM coupling [38] and Fluent-Rocky coupling [39]. Source terms are added to both continuity and momentum equations to account for the existence of the solid phase. On the other hand, Chu and Yu [40] implemented a CFD-DEM model in Fluent based on the formulation of model B [35]. It has been successfully applied in the study of various complex flow systems, such as fluidized bed [41,42] and cyclones separator [43, 44].

In the work report here a new model capable of addressing FSI problems in particle-fluid flows is proposed and developed. It incorporates a dynamic meshing method to fully resolve the effects of moving boundaries, and a six degrees of freedom solver to enable the motion of free objects to be captured. Its application as a customization to a commercial software framework allows for general application and simulation of complex industrial problems. In the present model, a single, large, free-moving object is considered. In analogy with discrete element modelling, the object's motion is tracked by Newton's second law of motion with a soft-sphere model used to treat object-structure collisions. For the first time, a dynamic meshing approach is combined with the conventional coupled CFD-DEM model to simultaneously resolve flow structures around the large free-moving object and to capture the behaviour of the small particles. The algorithm is fully implemented on the commercial software platform, ANSYS/Fluent, through its UDFs (user defined functions) due to its efficiency in handling dynamic meshing and complex geometries. The paper is organized as follows: a comprehensive model description is presented first, thereafter the validity of the model is examined by comparing the present simulation with literature data in different gas-fluidization systems. On this base, the capabilities of the present model in handling unstructured meshes and large, free-moving objects are demonstrated by analysing the dynamics of a fluidized system with an immersed tube that can be either fixed or free moving.

2. Model description and implementation

In the present study, the system consists of three major components: fluid, small particles and large objects. Accordingly, the fluid-solid interaction can be classified into two groups: fluid-small particle interaction and fluid-large object interaction, as schematically shown in Fig. 1. For the large object, the induced flow structure and its motion are resolved using a body-fitted dynamic meshing approach. The fluid forces acting on the object are calculated directly. On the other hand, the motion of small particles is modelled using an Euler-Lagrangian method which
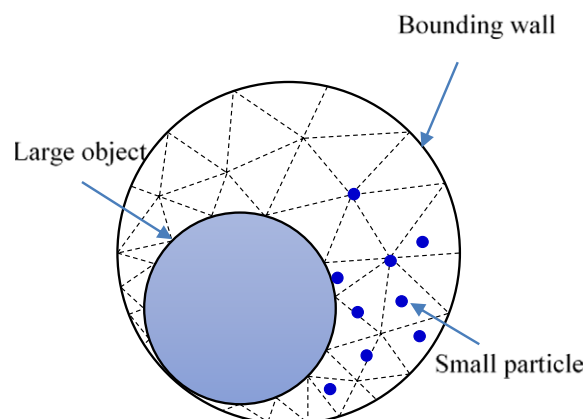

Fig. 1. Schematic demonstrating the modelling approach.

includes particle-particle collisions, this method is often referred to as a CFD-DEM approach. The CFD-DEM coupling between the two phases is achieved by the particle-fluid interaction at different scales: cell level for fluid phase and particle level for particulate phase. For the completeness, a brief description of the developed model for the fluid-solid interaction is given below.

2.1. Fluid phase

For the fluid phase, the governing equations are the same as those of the conventional Two Fluid Model (TFM) [45], referred as model A and have been adopted in Fluent as the Eulerian multiphase model, given as,

$$\frac{\partial\left(\varepsilon\rho_f\right)}{\partial t} + \nabla\cdot\left(\varepsilon\rho_f\boldsymbol{u}\right) = 0 \tag{1}$$

$$\frac{\partial\left(\varepsilon\rho_f\boldsymbol{u}\right)}{\partial t} + \nabla\cdot\left(\varepsilon\rho_f\boldsymbol{uu}\right) = -\varepsilon\nabla P - S_p + \nabla\cdot\left(\varepsilon\boldsymbol{\tau}_f\right) + \varepsilon\rho_f\boldsymbol{g} \tag{2}$$

where ρ_f, P, $\boldsymbol{\tau}_f$ and $\boldsymbol{g}$ are the fluid density, pressure shared by two phases, the viscous stress tensor and the acceleration due to gravity, respectively. ε is the volume fraction of fluid in each cell. S_p is the source term due to the rate of momentum exchange between the fluid phase and the particulate phase.

2.2. Solid phase

For the solid phase, both the large object and the small particles are treated as discrete elements whose motion can be described by Newton's second law of motion, written as,

$$m\frac{d\boldsymbol{v}}{dt} = \boldsymbol{F}_f + \boldsymbol{F}_c + m\boldsymbol{g} \tag{3}$$

$$I\frac{d\boldsymbol{\omega}}{dt} = \boldsymbol{T}_f + \boldsymbol{T}_c \tag{4}$$

where m, I, $\boldsymbol{v}$ and $\boldsymbol{\omega}$ are, the mass, inertia, translational and rotational velocities of the element, respectively. The force and torques acting on each element consists of several contributions, the hydrodynamic components, $\boldsymbol{F}_f$ and $\boldsymbol{T}_f$, arising from fluid-solid interaction, the collision components, $\boldsymbol{F}_c$ and $\boldsymbol{T}_c$, due to solid-solid interaction and gravity. If fine particles or cohesive particles are involved, other non-contact forces, such as van der Waals force and capillary force, have to be considered. The collisions between particles are handled by a soft-sphere model that allows for inter-particle overlap. The collision force includes the normal contact force $\boldsymbol{F}_n$, normal damping force $\boldsymbol{F}_{d,n}$, tangential contact force $\boldsymbol{F}_t$ and tangential damping force $\boldsymbol{F}_{d,t}$ while the collision torque $\boldsymbol{T}_c$ is composed of $\boldsymbol{T}_t$ caused by tangential force and $\boldsymbol{T}_r$ due to particle rolling friction resulting from the elastic hysteresis losses or viscous dissipation [46]. The calculation of collision forces is based on the magnitude of overlap, in which the normal contact behaviour is described by Hertz theory while the tangential elastic frictional contact is based on Mindlin and Deresiewicz theory [47]. Table 1 lists the equations used in the calculation. The details can be found elsewhere [48].

2.3. Phase coupling

The calculation of the fluid-solid interaction differs between the large objects and the small particles. For the large objects, the force and torque due to fluid flow are fully resolved at each CFD time-step, determined by the integration of fluid stress $\boldsymbol{\sigma}$ on its surface.

$$\boldsymbol{F}_f = \oiint\boldsymbol{\sigma}\cdot\hat{\boldsymbol{n}}dS \tag{5}$$

Table 1
Equations used to calculate forces and torques in this work.

Terms	Equation
Normal contact force	$\boldsymbol{F}_n = \frac{4}{3}E^*R^{*1/2}\delta_n^{3/2}\hat{\boldsymbol{n}}$
Normal damping force	$\boldsymbol{F}_{d,n} = -c_n(8m^*E^*\sqrt{R^*\delta_n})^{1/2}\boldsymbol{v}_n$
Tangential contact force	$\boldsymbol{F}_t = -\frac{\delta_t\mu_t|\boldsymbol{F}_n|}{|\boldsymbol{\delta}_t|}\left[1-\left(1-\frac{\min(|\boldsymbol{\delta}_t|,\delta_{t,max})}{\delta_{t,max}}\right)^{3/2}\right]$
Tangential damping force	$\boldsymbol{F}_{d,t} = -c_t\left(6\mu_t mE^*|\boldsymbol{F}_n|\frac{\sqrt{1-|\boldsymbol{\delta}_t|/\delta_{t,max}}}{\delta_{t,max}}\right)^{1/2}\times\boldsymbol{v}_t$
Torque due to tangential force	$\boldsymbol{T}_t = (\boldsymbol{F}_t + \boldsymbol{F}_{d,t})\times\boldsymbol{R}$
Rolling torque	$\boldsymbol{T}_r = \mu_r R|\boldsymbol{F}_n|\hat{\boldsymbol{\omega}}_n$

Where $1/R^* = 1/R_i + 1/R_j$, with R_i and R_j being the radius of two particles in contact, $1/E^* = (1-\nu_i^2)/E_i + (1-\nu_j^2)/E_j$, with E and ν the Young's Modulus and Poisson's ratio, respectively; δ_n and $\boldsymbol{\delta}_t$ represent the overlap in normal and tangential directions; $\delta_{t,max} = \mu_t((2-\nu)/(2-2\nu))\delta_n$, with μ_t the sliding friction and μ_r the rolling friction; $\hat{\boldsymbol{\omega}}_n = \boldsymbol{\omega}_n/|\boldsymbol{\omega}_n|$ with $\boldsymbol{\omega}_n$ the angular velocity; $c_n = -\ln e/\sqrt{\pi^2 + \ln^2 e}$ with e the restitution coefficient (e is defined as the ratio of post-collisional contact velocity to pre-collisional contact velocity) and c_t is the tangential damping coefficient.

$$\boldsymbol{T}_f = \oiint\boldsymbol{R}\times(\boldsymbol{\sigma}\cdot\hat{n})dS \tag{6}$$

However, for the small particles, forces caused by fluid flow are modelled. The fluid-particle interaction is resolved at the fluid cell level. The total fluid-particle interaction force can be split into a pressure gradient force and a drag force.

$$\boldsymbol{F}_f = -V_p\nabla P + \boldsymbol{F}_d \tag{7}$$

where V_p, ∇P and $\boldsymbol{F}_d$ are, respectively, the volume of the particle, pressure gradient and drag force. The particle drag force $\boldsymbol{F}_d$ is determined by cell-averaged porosity, flow velocity and particle velocity, given as,

$$\boldsymbol{F}_d = \frac{\beta V_p}{1-\varepsilon}(\boldsymbol{u}-\boldsymbol{v}) \tag{8}$$

with β the interphase momentum exchange coefficient.

To test the impact of drag model on bubbling behaviour, drag model proposed by Beetstra et al. [49] and drag model of Ergun and Wen & Yu [50,51] are used in this work. The Beetstra model is derived from Lattice-Boltzmann simulation and is valid over a wide range of Reynolds numbers. Accordingly, the interphase momentum exchange coefficient, β, is given as,

$$\beta = A\frac{\mu}{d^2}\frac{(1-\varepsilon)^2}{\varepsilon} + B\frac{\mu}{d^2}\frac{1-\varepsilon}{\varepsilon}Re_p \tag{9}$$

in which the particle Reynolds number Re_p is defined as $Re_p = \rho d_p\varepsilon|\boldsymbol{u}-\boldsymbol{v}_p|/\mu$. The coefficient $A = 180 + 18\varepsilon^4(1+1.5\sqrt{1-\varepsilon})/(1-\varepsilon)$ and coefficient $B = 0.31(\varepsilon^{-1} + 3\varepsilon(1-\varepsilon) + 8.4Re_p^{-0.343})/(1+10^{3(1-\varepsilon)}Re_p^{2\varepsilon-2.5})$. On the other hand, the drag model of Ergun and Wen & Yu is based on experimental measurements. The interphase momentum exchange coefficient, β, is given as,

$$\beta = \begin{cases} 150\frac{\mu(1-\varepsilon)^2}{\varepsilon d_p^2} + 1..75\frac{(1-\varepsilon)\rho_f}{d_p}|\boldsymbol{u}-\boldsymbol{v}_p| & (\varepsilon<0.8) \\ \frac{3}{4}C_D\frac{\varepsilon(1-\varepsilon)}{d_p}\rho_f|\boldsymbol{u}-\boldsymbol{v}_p|\varepsilon^{-2.65} & (\varepsilon>0.8) \end{cases} \tag{10}$$

where $C_D = 24(1.0+0.15Re_p^{0.687})/Re_p$ when $Re_p < 1000$ and $C_D = 0.44$ when $Re_p > 1000$.

The rate of momentum exchange in the right of Eq. (2) is calculated by summing up the drag force acting on particles in a fluid cell so that Newton's third law of motion is satisfied [13], given by,

$$S_p = \frac{1}{V_{cell}}\sum_{n=1}^{N_{pc}}\frac{\beta V_p(\boldsymbol{u}-\boldsymbol{v}_p)}{1-\varepsilon} \tag{11}$$

with V_{cell} being the volume of a fluid cell and N_{pc} the number of particles in the fluid cell.

In CFD calculation, flow properties, such as velocity, pressure and its gradients, are normally stored at the cell centre. To calculate the fluid force, Eulerian properties at the fluid cell level needs to be mapped to the particle position. To this end, a linear interpolation is employed in the present work. Flow property at the particle position is determined as,

$$\phi_p = \phi_{cell} + \nabla \phi_{cell} \cdot dr \tag{12}$$

where ϕ_p and ϕ_{cell} are the fluid properties at particle position and the cell centre; dr is the distance vector directing from cell centre to particle position. The gradient of fluid property $\nabla \phi_{cell}$ at each cell is calculated using the divergence theorem [22],

$$\nabla \phi_{cell} = \frac{1}{\Delta V} \sum_f^{N_{face}} \phi_f A_f \tag{13}$$

with ϕ_f being the fluid property at each face calculated by averaging from two cells adjacent to the face.

2.4. Implementation on ANSYS Fluent

Commercial CFD code, ANSYS Fluent v17.1, has been used as the modelling platform which solves the Navier-Stokes equations based on FVM. The use of ANSYS/Fluent allows us to handle internal large object with complex geometries and the re-meshing process can be handled efficiently. To accurately describe the induced flow structure, the computational mesh is composed of two parts: prism boundary layer attached to the surface of the moving large object and tetrahedral part containing the rest of the domain. The body-fitted tetrahedral mesh is used due to its compatibility with the dynamic meshing. *Re*-meshing is triggered only when the skewness and size of the mesh exceed specified thresholds. Consequently, flow field around the large object is fully resolved. The present model can overcome the inaccuracy caused by staircase approximation of the moving boundary. The force and torque on the large object due to fluid flow are calculated by integrating pressure and viscous stress over the surface of the large object. Meanwhile, collision with small particles and bounding walls are explicitly modelled by the soft-sphere DEM model. Consequently, the large object interacts explicitly with fluid flow, bounding walls and small particles. The motion of large object is described by Newton's law of motion, like that of small particles but using a time-step same as that of the CFD calculation. Therefore, CFD time-step is also affected by the mass, size and stiffness of the large object. At the end of each CFD time-step, the updated linear and angular velocity are assigned to the large object as a boundary condition. The displacement of the large object is then enforced by the CFD solver and is accommodated by dynamic meshing, thus leading to a two-way coupling between the fluid flow and the large object.

The coupling between fluid and the small particles, on the other hand, are implemented by first performing the CFD calculation for one CFD time-step and subsequently evaluating the fluid forces acting on individual particle based on the updated flow field. Particles are then advanced at a smaller DEM time-step until synchronized with the CFD time, yielding updated particle information, such as particle position and velocity. These information are then used to renew volume fraction at each fluid cell and to update momentum exchange term for the CFD calculation at next time-step. This calculation cycle continues until reaching the total simulation time. In general, the present model takes advantage of the conventional CFD-DEM approach whilst capturing the dynamic of the large object in particle-fluid flows.

The algorithm is implemented in Fluent based on the Eulerian multiphase model by means of its User Defined Functions (UDFs). Fig. 2 shows the flow chart of the algorithm of the UDFs which are called at the end of each CFD time-step through macro DEFINE_EXECUTE_AT_END. User defined memories (UDMs) are used to store cell-based information, including the volume fraction and the momentum exchange terms. The implemented algorithm supports both serial and parallel calculation of the flow field. For the small particles, the DEM loop for the small particles may be executed multiple times due to the difference in time-steps between CFD and DEM calculation. To calculate fluid force acting on the small particles, the CFD cell in which the particle of interest resides needs to be identified in order to map the Eulerian properties to the small particles. For parallel computing, particle properties, including position, velocity and diameter, are first broadcast from host to node. Searching of the cell is then conducted by using macro DPM_Locate_Point together with macro DPM_Init_Oct_Tree_Search for initialization and DPM_End_Oct_Tree_Search for clean-up of the memory. Both the initialization and clean-up are called at every CFD time-step only if the dynamic meshing is enabled. The dynamics of the large object, translational and rotational velocities, are fed back to the Fluent through macro DEFINE_CG_MOTION while the momentum sources are added to the governing equations by macro DEFINE_SOURCE.

3. Results and discussion

To develop confidence in the proposed model, it is essential to validate against well-defined experiments. In the present study, two different fluidized bed test cases are adopted for this purpose. The first case tests the validity of the developed CFD-DEM method implemented in Fluent by comparing the predicted time-averaged velocity and porosity profiles with both experiments and previous simulations. The second case tests the capability of the present model in the prediction of bubble formation and propagation in a spouted bed and evaluates the performance of two alternative drag models. The ability of the model to deal with a large object is then demonstrated by simulating a fluidized bed with an immersed tube. Initially the tube is kept stationary in order to confirm the capability of the present model in handling an unstructured mesh. The tube is then allowed to move freely and the capability of the present model to address a free-body FSI problem in a dispersed particle-fluid flow is demonstrated.

For all the simulated cases, phase coupled SIMPLE scheme was used for pressure-velocity coupling. The least squares cell based gradient method was adopted for gradient while QUICK scheme was used for momentum. The method has second order of accuracy in both time and space. The gas flow was introduced uniformly from the bottom of the fluidized bed by means of a velocity-inlet boundary condition. The top of the bed was specified as pressure outlet while no-slip boundary conditions were applied to the bounding walls. At each time-step, the residual for each governing equation was controlled below 10^{-5} for convergence. In this study, the turbulent gas flow is modelled by the standard k-epsilon model since the impact of turbulence on the velocity filed is minor for dense particle flow [28].

3.1. Fluidized bed

A fluidized bed with dimension of 44 mm × 10 mm × 120 mm was simulated, for which time-averaged porosity distribution [52] and velocity profiles of the particles [53] measured by magnetic resonance (MR) are available. The drag law of Beetstra [49] derived from Lattice Boltzmann simulation is adopted here to simulate the fluidization of poppy seeds in their experiments, as it gives a slightly better predictions according to a comparison made by Muller et al. [52].

The parameters used for the simulation are summarized in Table. 2. For convenience, the wall's material properties are the same as the particle's but with an infinitely large contact radius when handling particle-wall collision. The computational domain is discretised into a uniform hexahedral mesh with 12 × 3 × 30 cells, giving a mesh size that is at least 2.7 times the particle size. Non-overlapping particles are initially generated randomly in the domain and fall under the
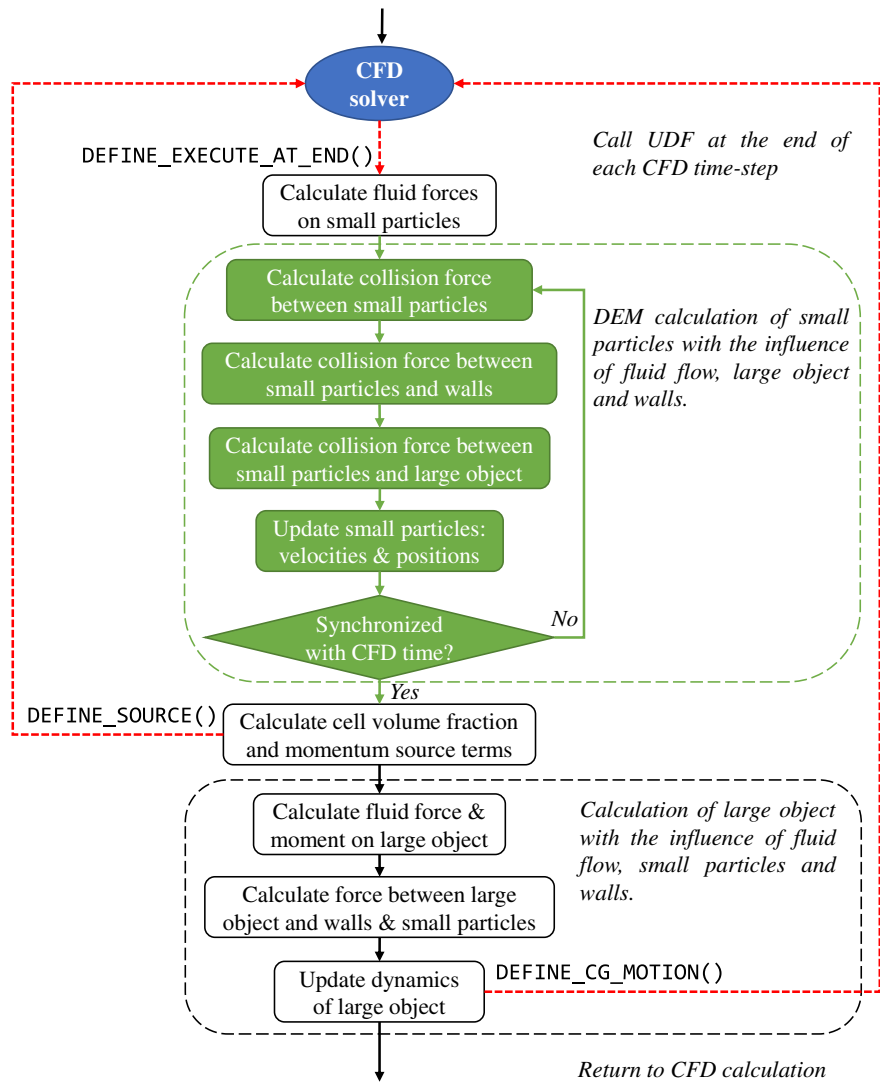
Fig. 2. Flow chart of the algorithm of the UDF implementation of the CFD-DEM coupled with dynamic meshing approach.

influence of gravity to form a packed bed. The bed is then fluidized with a superficial gas velocity of 0.9 m/s, corresponding to 3 times the minimum fluidization velocity. A total physical time of 20 s is simulated. Transient results are recorded every 10 ms for post-processing.

The pressure drop across the fluidized bed is a critical parameter normally used to determine the minimum fluidization velocity. Fig. 3 shows the temporal variation of pressure drop normalized by the pressure caused by bed weight. The pressure drop reflects the dynamic behaviour of the bed. It rises sharply shortly after introducing the fluidizing gas and then falls rapidly and fluctuates around the value of 1.0. The fluctuations of the pressure drop are an indication of the bubbling behaviour, as bubbles repeatedly emerge from the bottom and travel through the bed before erupting at the top.

The bubbling behaviour is readily revealed by the particle flow pattern. The general observations are similar as those reported by Muller

Table 2
Parameters used in simulation.

| Parameters	Value
Particle number, N_p	9240
density, ρ_p (kg/m^3)	1000
Particle diameter, d_p (mm)	1.2
Young's modulus, E (Pa)	1.0×10^8
Poisson ratio, ν	0.3
Rolling fiction coefficient, μ_r	0.2
Sliding friction coefficient, μ_t	0.1
Normal restitution coefficient, e_n	0.98
Tangential damping coefficient, c_t	0.02
Temperature of gas, T_g (K)	298
Viscosity of gas, μ_g (kg/(s·m))	1.8×10^{-5}
Superficial gas velocity, v_g (m/s)	0.9
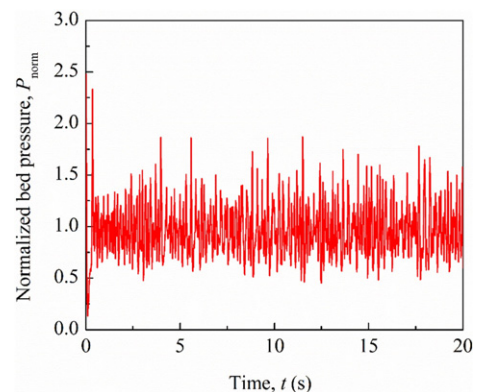
Fig. 3. Normalized bed pressure drop during fluidization with air velocity of 0.9 m/s.

et al. [52]. The fluidization quickly stabilizes and a repeatable particle flow pattern is clearly observed. A single bubble grows on the distributor plate before detaching, the particles rising on top of the bubble and falling back under gravity as it passes. A typical representation of the bubble is shown in Fig. 4a, in which a single, large bubble can be seen. As pointed out by Muller et al. [52], this bubbling behaviour is mainly caused by the fairly small size of the bed. A snapshot of the particle velocities corresponding to Fig.4a is shown in Fig. 4b. For clarity, only particles located in the 1.2 mm thick central slice of the bed are shown. It can be seen that particles are moving upward in the central region while downward in the vicinity of the walls. This typical core-annular flow pattern captured by the present simulation agrees with the previous results reported [52]. The corresponding gas behaviour is presented in Fig. 4c. The vector represents the direction of gas flow while the contour denotes the magnitude of the gas velocity. Again, the gas behaviour observed by Muller et al. [52] is qualitatively captured by the present simulation, in which the gas moves upwards quickly in the bubble region and recirculates at the left and right side of the bubble.

To make a quantitative comparison, time-averaged volume fraction and particle velocity is extracted and compared. The numerical results during the start-up period, approximately 3 s, are excluded to make a statistically meaningful comparison with the experiments. Fig. 5 compares the time-averaged porosity profiles with both experiments and CFD-DEM results reported in Muller et al. [52] at two heights above the distributor plate: 16.4 and 31.2 mm. In general, the present results are comparable with the experimental data but slightly over-predict the porosity especially in the vicinity of the side walls, similar findings are also reported in other validation tests of CFD-DEM methods [54, 55]. At the height of 16.4 mm, the maximum difference between the predicted values and the experimental values is within 20% relative to the experimental value. At the height of 31.2 mm, the difference is smaller than 10% in the middle part of the bed while slightly larger than 10% near the side walls. Compared to the simulation results of Muller et al. [52], the present prediction is closer to the experimental data. However, it should be noted that the present simulation shows slightly large porosities in the central region of the bed than that of the results predicted by Muller et al. [52]. It can be attributed to the additional rolling resistance introduced by the rolling friction model adopted in the present simulation. Therefore, less kinetic energy is consumed by particle rotation and more energy is transformed into translational motion. However, the particles in the current simulation belong to Geldart's Group D, consequently their behaviour is mainly dominated by the gas hydrodynamics.
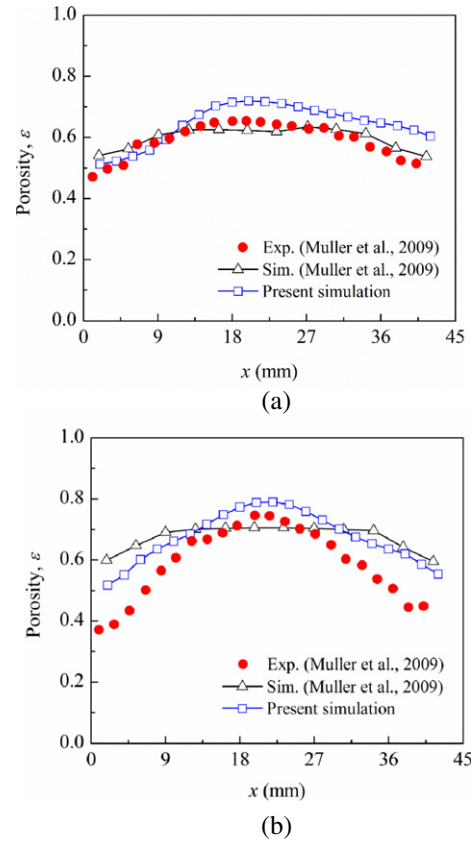

(a)

(b)

Fig. 5. Comparison of time-averaged porosity profiles for a superficial velocity of 0.9 m/s at different heights: (a) 16.4 mm and (b) 31.2 mm.

Further validation is made against the time-averaged vertical particle velocity. Fig. 6 compares the time-averaged velocity profile of particles with experiments at three different heights: 15 mm, 25 mm and 35 mm. A better match in the central region is obtain by the present model than that of the CFD-DEM simulation in [53]. The major difference with the experimental observation is the up-turning tail of velocity profile in the vicinity of the side walls. This discrepancy may be related to factors like the use of spherical particle shape instead of real shape of the poppy seeds, particle-wall collision model, mesh resolution and

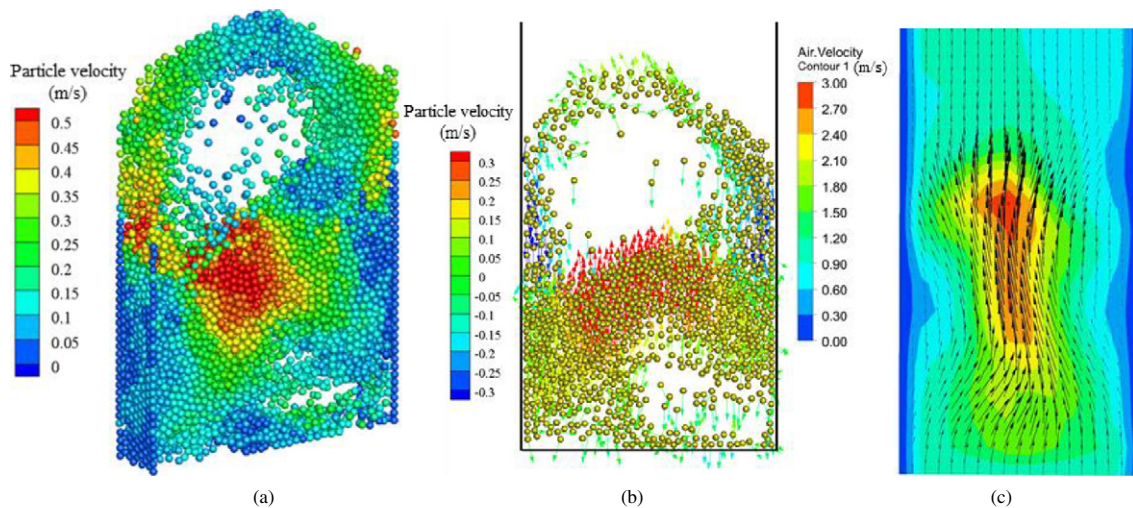(a)   (b)   (c)

Fig. 4. (a) A typical bubble, in which particles are coloured by the magnitude of velocity; (b) snapshot of the vertical velocity of particles in the bubbling fluidized bed. Only particles with centres located in the 1.2 mm thick central slice of the bed are shown; (c) snapshot of the gas velocity in the middle plane of the bed. The fluidization velocity is 0.9 m/s.
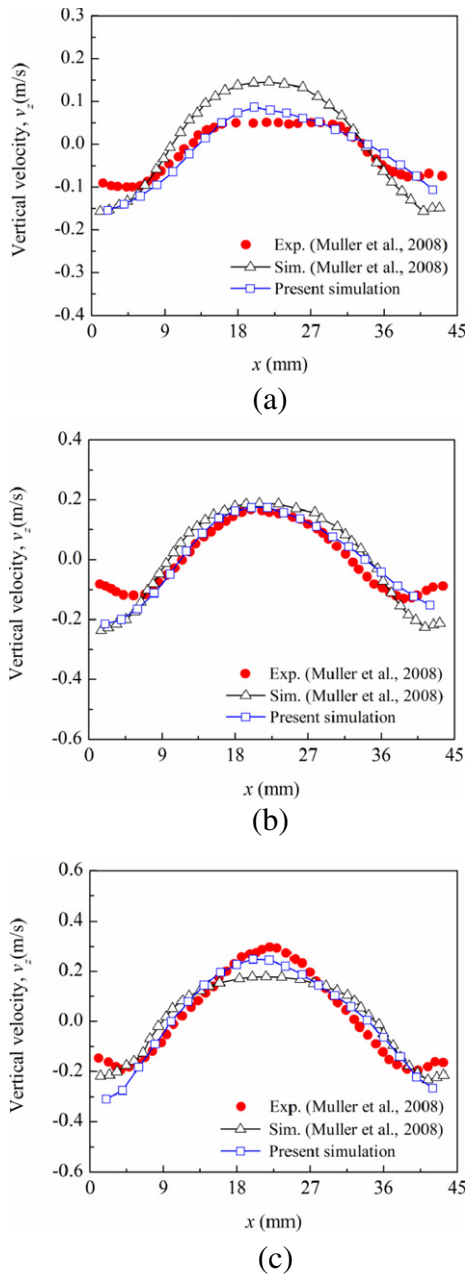
Fig. 6. Comparison of profiles of vertical velocity of particles at different heights of the bed: (a) 15 mm, (b) 25 mm and (c) 35 mm.

turbulence modelling. A drag model which considers the effect of particle shape is expected to improve the numerical prediction. In general, both the qualitative and quantitative agreement confirms that the present model has captured the key feature of this fluidization system, which verifies our CFD-DEM method on the platform of Fluent.

3.2. Spout-bed

The mixing and segregation behaviour of fluidized bed are found to be strongly influenced by bubble characteristics and dynamics [56]. In this section, the capability of the present model in the prediction of bubble formation and propagation is tested in a spout bed. A single bubble is injected in a pseudo-2D fluidized bed at incipient fluidization conditions. Comparisons with experimental data obtained by Particle Image Velocimetry (PIV) are made in terms of bubble shape and velocity profile of the particles around the bubble. The experiments were performed

Table 3
Parameters used in simulation.

Parameters	Value
Particle number, N_p	30,000
Density, $\rho_p (kg/m^3)$	2526
Particle diameter, d_p (mm)	2.5
Young's modulus, E (Pa)	1.0×10^8
Poisson ratio, ν	0.3
Rolling fiction coefficient, μ_r	0.02
Sliding friction coefficient, μ_t	0.2
Normal restitution coefficient, e_n	0.97
Tangential damping coefficient, c_t	0.33

by Bokkers et al. [56] in a bed with dimensions of $15 \times 150 \times 1000$ mm and with a central jet of 10 mm width. A total number of 30,000 glass beads of 2.5 mm diameter are used in the simulation. The computational domain is discretised into hexahedral mesh with $15 \times 3 \times 45$ cells. Other simulation parameters are listed in Table 3. The simulation starts with random generation of particles in the rectangular box, followed by particle packing under gravity until velocities of all particles are negligible. Then, a jet at a velocity of 20 m/s is injected from the central orifice for a duration of 0.15 s while introducing background gas at a velocity of 1.2 m/s uniformly from the rest of the bottom.

To examine the influence of drag model on the bubble shape, two different drag models are considered: the drag model of Beetstra [49] as used above and the drag model of Ergun and Wen & Yu [50,51]. To ensure the results are comparable, both cases are started from the same packing condition. The bubble formation shows dependence on the drag model, which can be readily demonstrated by the particle flow pattern. Fig. 7 shows the particle distributions during single bubble injection at different times predicted by two drag models, in which particles are coloured by the vertical velocity. Following an initial expansion, the bubble gradually grows in size and moves upward over time. The interface between the top of the bubble and the bed predicted by the Beetstra model is less clear and less defined compared to that of
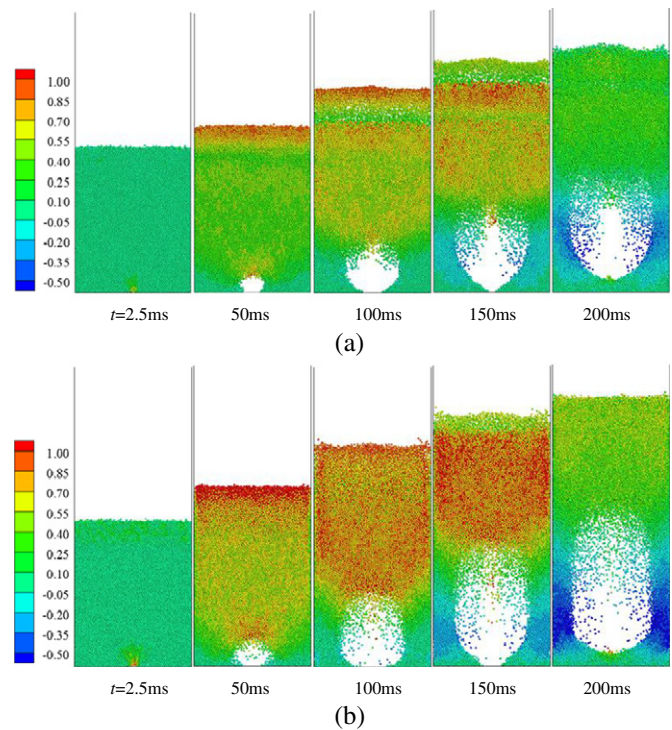

Fig. 7. Particle distribution in the spout bed predicted by (a) the drag model of Beetstra [49] and (b) the Ergun and Wen & Yu drag model at different times. Particles are coloured by the vertical velocity.
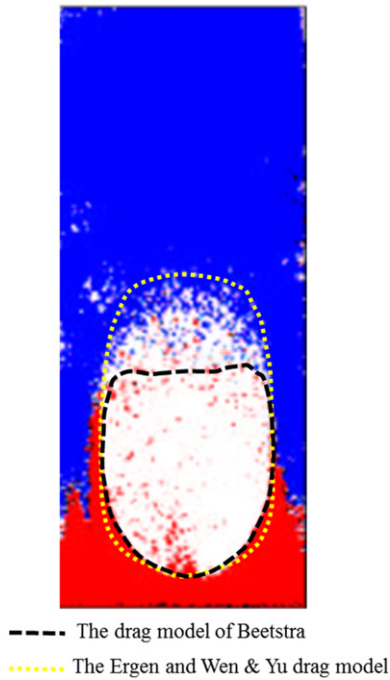
Fig. 8. Comparison of bubble size predicted by different drag models with experiment. The bubble is defined by a critical solid volume fraction of 0.2. Coloured layers of particles are used in the experiment [56].

the Ergun and Wen & Yu drag model. In Fig. 8, the bubble profile is defined using a critical solid volume fraction of 0.2 and compared with that obtained from experiment at 200 ms [56]. It can be seen that the bubble size is under-predicted by the Beetstra drag model and slightly over-predicted by the drag model of Ergun and Wen & Yu. In addition, the drag model of Ergun and Wen & Yu give a bed expansion closer to that of the experiments. Bokkers et al. [56] compared the drag model of Ergun and Wen & Yu with the drag model of Koch and Hill which is derived from LBM simulation. Similarly, they found that the drag model of Ergun and Wen & Yu gives a slightly larger bubble and less diffuse interface between the air bubble and the particles.

Fig. 9 shows the vector plot of particle velocity for the two cases. The overall trends in the two cases are similar. The particles around the bubble are being pushed outwards and are deflected in the horizontal direction, making particles moving upwards and downwards along the side

walls. Particles in the wake of the air bubble move towards the central orifice to fill the space behind the rising air bubble. Two re-circulations are formed in the bottom corners of the bed. The major difference lies in the particle velocities above the bubble with a much higher magnitude using the Ergun and Wen & Yu drag relations, leading to a larger bubble size than that of the Beetstra model [49]. To sum up, the qualitative agreement with experiment confirms the capability of the present model in predicting bubble formation and propagation in a spout bed. The comparison between two drag models further illustrates that the bubble size depends on the selection of drag model.

3.3. Fluidization with immersed tube

3.3.1. Fluidization with a stationary tube

In gas-fluidized bed, immersed tubes are often used to effectively remove/provide heat from/to the bed. The existence of immersed tube has a significant impact on the particle behaviour and heat transfer. Extensive experimental studies have been conducted in this regard [10,57,58]. In this section, a pseudo-2D fluidized bed with an immersed tube is simulated. The purpose of this case is to demonstrate the capability of the present model in handling an unstructured mesh. The fluidized bed has dimensions 10 mm × 88 mm × 200 mm, in which a stationary tube with diameter of 24 mm is fixed at a height of 60 mm. The geometry and grid representation used in the simulation are illustrated in Fig. 10. The whole domain is discretised into tetrahedral meshes with a volume at least 3 times larger than that of a particle. In order to better capture the flow structure, the mesh size in the boundary layer on the tube is much smaller than particle size. In order to improve stability of CFD calculation, a similar procedure in [42] was adopted here to limit the solid volume fraction to 0.64 (typical random loose packing density) and redistribute source terms to neighbour cells. A total number of 20,000 particles are generated randomly without overlap above the tube to form a packed bed under gravity. The gas is then introduced uniformly from the bottom at a constant velocity of 0.9 m/s to fluidize the bed. Other material properties used in the simulation can be found in Table 2.

Fig. 11 shows the particle flow pattern during the initial stage of fluidization. Particles are coloured by velocity magnitude. Particle behaviour, especially the bubble characteristic, is strongly affected by the presence of the immersed tube. Shortly after introducing the gas, the particle flow is being divided and accelerated passing through the gap between the tube and the side walls, forming a stagnant region right below the tube (Fig. 11a). Then, due to the collision between particles and the tube, an air film with varying thickness is formed blow the
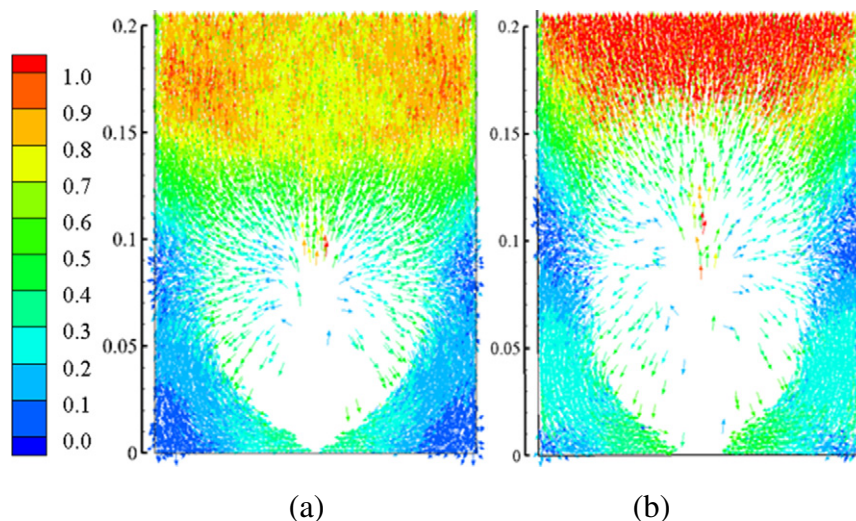

Fig. 9. Vector plot of particle velocity in spout bed by (a) drag model of Beetstra and (b) Ergun and Wen & Yu drag model.
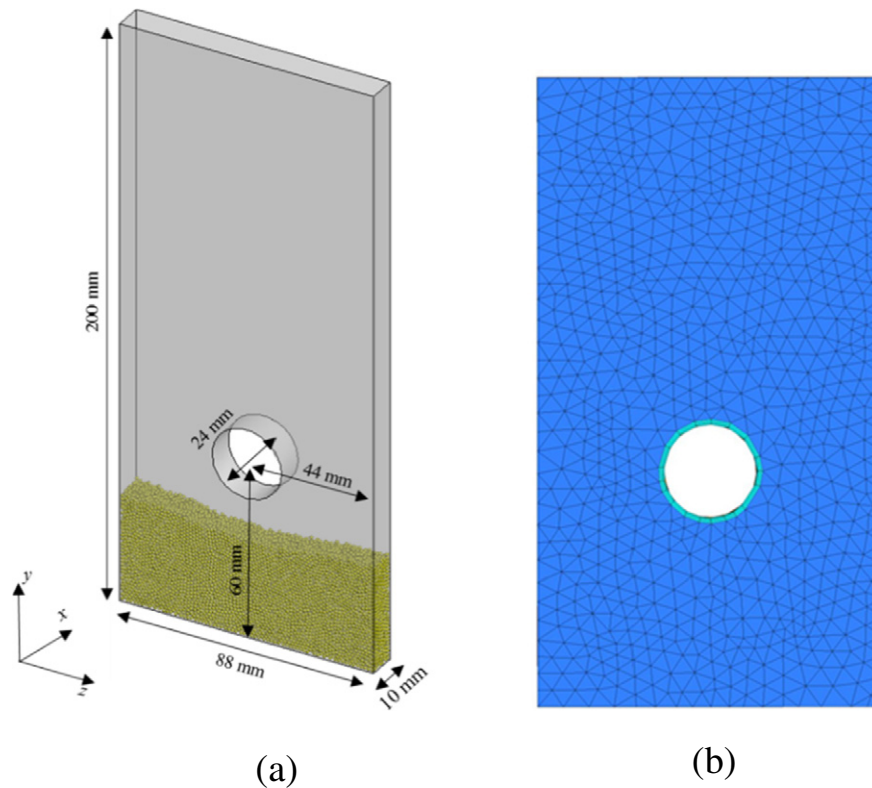
Fig. 10. (a) Geometrical and (b) numerical grid representation of the fluidized bed with an immersed tube.

tube (Fig. 11b). Under the influence of gravity, an air bubble gradually grows in size underneath the tube (Fig. 11c). As fluidization continues, defluidized particles fall back, forming a stagnant region on top of the tube. Meanwhile, the particles close to the distributor plate starts to fluidize again, leading to a reduction of bubble size below the fixed tube (Fig. 11d). The formation of an air film below the tube and a stagnant region above the tube qualitatively agree with both experimental observation [59] and numerical simulation [32], thus confirming the capability of the present model in dealing with an unstructured mesh.

3.3.2. Fluidization with a free-moving tube

In order to demonstrate the key capability of the present model, namely its ability to model a large dynamic object, the previous case is extended by allowing the immersed tube to move freely. The numerical setup is the same as the previous case, except that the density ratio between moving tube and particles is set to 1.0. The upper and lower thresholds of the cell size are set as 1.2 and 0.8 times of the averaged size in the initial mesh. The threshold value of skewness for re-meshing is set to 0.75 to maintain an acceptable mesh quality.

Since the tube is free-moving, its motion is determined by the combined effect of gas flow, collision with small particles and confinement of the side walls. The motion of the tube will conversely introduce change to the fluid field, further increasing the complexity of the system. Fig. 12 shows the evolution of the particle flow pattern after fluidization is started. Particles are coloured by velocity magnitude. The tube sinks down shortly after the fluidization has started and bounce back
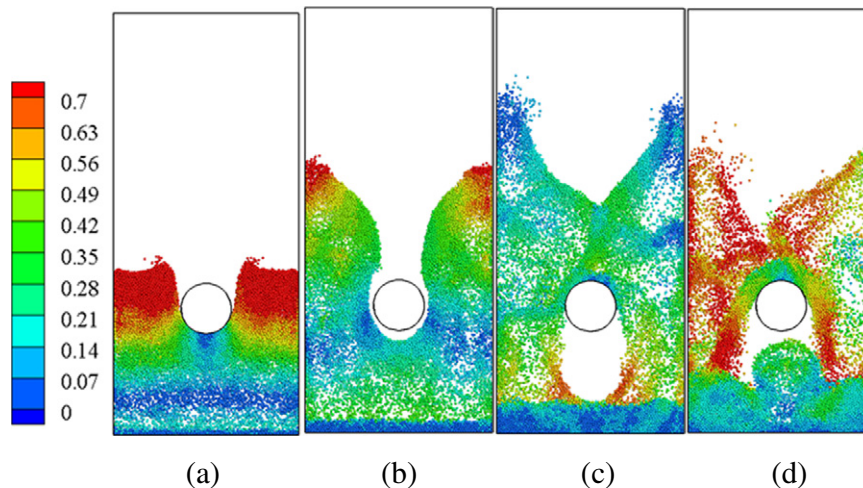

Fig. 11. Particle distribution in a fluidized bed with an immersed tube at different times: (a) $t = 0.07$ s; (b) $t = 0.12$ s; (c) $t = 0.20$s and (d) $t = 0.28$ s. Particles are coloured by velocity magnitude.
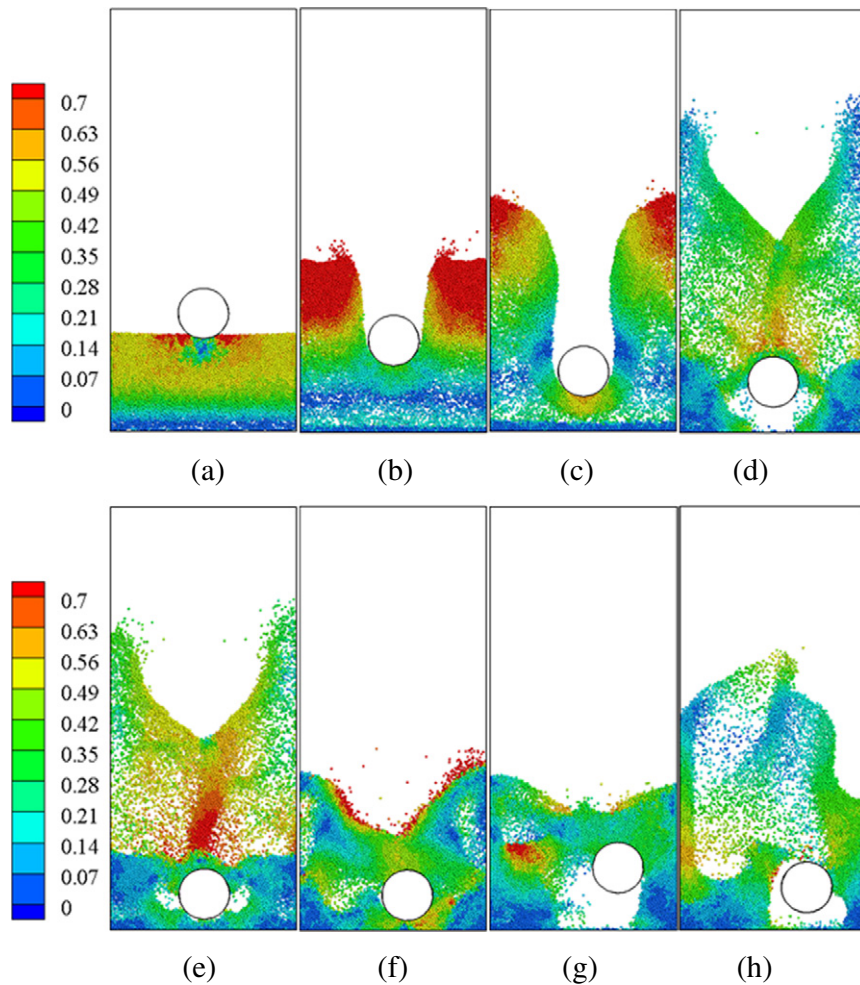
Fig. 12. Particle distribution in a fluidized bed with an immersed free-moving tube at different times: (a) $t = 0.03$ s; (b) t = 0.07 s; (c) t = 0.10s; (d) t = 0.20s; (e) $t = 0.23$ s, (f) $t = 0.33$ s, (g) $t = 0.39$ s and (h) $t = 0.52$ s. Particles are coloured by velocity magnitude.

and forth due to collision with the bounding walls. In contrast to the fixed tube, there is no air film forming under the tube, as shown in Fig. 12b. The particles below the tube are pushed downwards by the falling tube, forming a thick layer of particles below the tube. Meanwhile, other particles are being dragged up by the fluidizing gas. In Fig. 12d, shortly after the tube has hit the distributor plate, a clear gas bubble forms between the tube and the plate. The presence of the tube causes the bubble below it to split into two smaller bubbles with one on each side of the tube (Fig. 12e). The bubble on the right side of the tube gradually disappears as the tube begins to move towards right and particles fall down under gravity. As fluidization continues, an air bubble is produced again behind the tube after it is being blown up by the gas (Fig. 12g). Due to combined effect of fluidization and the effect of the moving tube on the gas flow, large air bubbles are repeatedly formed adjacent to the tube throughout the process (Fig. 12e).

The present model permits us to not only monitor the variations in position and velocity of the internal structure but also enables a detailed understanding of its dynamics. Fig. 13 shows the time history of the motion and fluid force of the immersed tube during fluidization. Only vertical positons are shown here. The fluid force on the tube is normalized by the magnitude of the force due to gravity. It can be seen, for these conditions, that there is an oscillation in the vertical position of the tube. The sudden jump in the velocity is caused by the collision with the bounding walls. One distinct advantage of the present model is to allow the internal structure to rotate due to the fluid-structure interaction, wall collision and particle-structure interaction. In this case, the

change in the angular momentum is mainly caused by collision with the fluid bed's walls (Fig. 13c). As shown in Fig. 13d, the magnitude of fluid force acting on the tube is lower than that of gravity and the fluctuations in this force are due to the bouncing motion of the tube with a magnitude significantly smaller than that of gravity, implying that the motion of the tube is dominated by the gravity and the collision with bounding walls. Although the discussion is purely based on a numerical study, the predicted dynamics highlight the complexity of the interactions in these systems. The unsteady, coupled, gas flow and particle flows, and tube-wall collisions, all playing a significant role in the behaviors observed. Clearly, it is very important to resolve the flow around the free object and accurately capture the collision dynamics when modelling systems with large objects in particle fluid flows.

4. Conclusions

In this study, a new numerical model was developed to tackle free-body fluid-structure interaction problems in particle-fluid flows, in which a conventional CFD-DEM method was combined with a dynamic meshing approach. The flow structure induced by the large free-moving object was directly resolved by a body-fitted mesh while the dynamic meshing was utilized to accommodate the large object's motion, thus achieving a two-way coupling between the large object and fluid flow. On the other hand, the behaviour of small particles were captured by a coupled CFD-DEM method in which the fluid-particle interaction was model by a drag correlation. By treating the large moving object
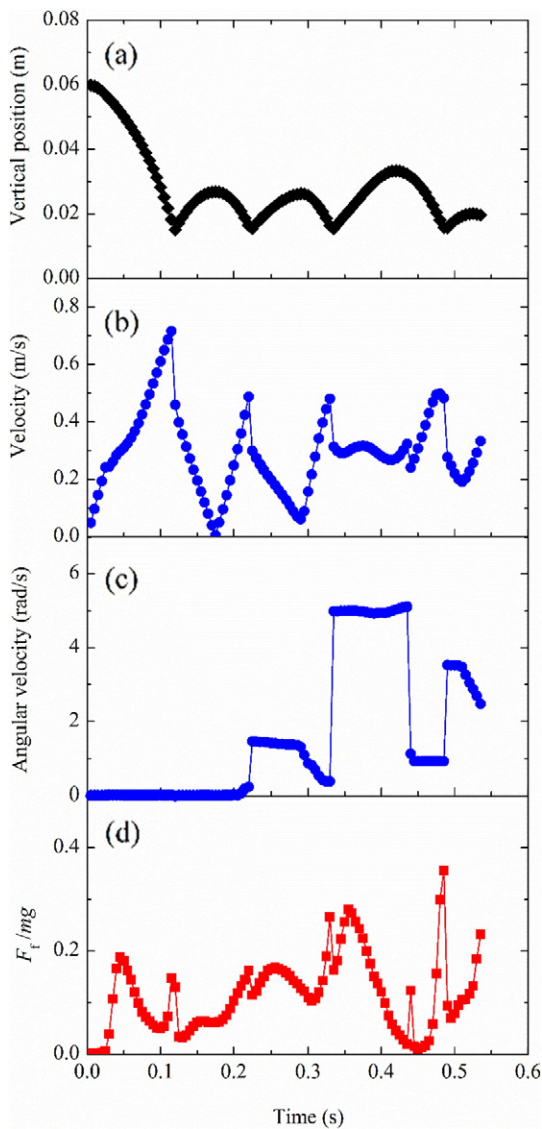
Fig. 13. Vertical position, velocity, angular velocity and fluid force acting on the tube during fluidization.

as a single element, its collision with small particles and bounding walls are handled by a soft-sphere DEM model. The proposed model has been fully implemented on a commercial software platform, ANSYS/Fluent, through its UDFs, thus allowing for the efficient handling of dynamic meshing and general application to industrial systems with complex geometries.

Validation of the CFD-DEM method has been conducted both qualitatively and quantitatively against available literature data in the cases of fluidization. The profiles of time-averaged porosity and velocity show a good quantitative agreement with experimental measurements on a gas fluidized bed. The predicted dynamics of bubble growth in a spout bed were shown to depend on drag model used, the Ergun and Wen & Yu model gave a good agreement with experiment. The characteristic particle flow patterns in a fluidized bed with a fixed tube were also captured, confirming the capability of the present model in handling an unstructured mesh. The model's ability to predict fluid-structure interaction in particle-fluid flow was demonstrated by a fluidization case allowing the tube to move freely. The predicted interacting dynamics of the gas, particle and tube were highly complex and highlighted the value of fully resolving the flow around the large object.

The present model shows strong potential in modelling particle-fluid flows with complex and/or free-moving large objects, such as milling, drug delivery and agitated chemical reactors. It enables a fully-resolved flow field around the moving objects but at the cost of additional computational time due to the dynamic meshing. Its application to an agitated tubular reactor with a free-moving internal agitator will be reported in the future. Experimental validation on the forced motion of the internal agitator and the induced flow field will be examined in more detail.

Acknowledgement

References

[1] R.R. Cai, Y.G. Zhang, Q.H. Li, A.H. Meng, Experimental characterizing the residence time distribution of large spherical objects immersed in a fluidized bed, Powder Technol. 254 (2014) 22–29.

[2] Y. Zhang, B.S. Jin, W.Q. Zhong, Experimental investigation on mixing and segregation behavior of biomass particle in fluidized bed, Chem. Eng. Process. 48 (2009) 745–754.

[3] H.P. Cui, J.R. Grace, Fluidization of biomass particles: a review of experimental multiphase flow aspects, Chem. Eng. Sci. 62 (2007) 45–55.

[4] D.L. Browne, B.J. Deadman, R. Ashe, I.R. Baxendale, S.V. Ley, Continuous flow processing of slurries: evaluation of an agitated cell reactor, Org. Process. Res. Dev. 15 (2011) 693–697.

[5] G. Gasparini, I. Archer, E. Jones, R. Ashe, Scaling up biocatalysis reactions in flow reactors, Org. Process. Res. Dev. 16 (2012) 1013–1016.

[6] C. Tangsathitkulchai, Acceleration of particle breakage rates in wet batch ball milling, Powder Technol. 124 (2002) 67–75.

[7] C. Tangsathitkulchai, L.G. Austin, Slurry density effects on ball milling in a laboratory ball mill, Powder Technol. 59 (1989) 285–293.

[8] N. Islam, E. Gladki, Dry powder inhalers (DPIs) - a review of device reliability and innovation, Int. J. Pharm. 360 (2008) 1–11.

[9] H. Bai, J. Theuerkauf, P.A. Gillis, P.M. Witt, A coupled DEM and CFD simulation of flow field and pressure drop in fixed bed reactor with randomly packed catalyst particles, Ind. Eng. Chem. Res. 48 (2009) 4060–4074.

[10] S.W. Kim, J.Y. Ahn, S.D. Kim, D.H. Lee, Heat transfer and bubble characteristics in a fluidized bed with immersed horizontal tube bundle, Int. J. Heat Mass Transf. 46 (2003) 399–409.

[11] A.O.O. Denloye, J.S.M. Botterill, Bed to surface heat-transfer in a fluidized-bed of large particles, Powder Technol. 19 (1978) 197–203.

[12] B.P.B. Hoomans, J.A.M. Kuipers, W.J. Briels, W.P.M. van Swaaij, Discrete particle simulation of bubble and slug formation in a two-dimensional gas-fluidised bed: a hard-sphere approach, Chem. Eng. Sci. 51 (1996) 99–118.

[13] B.H. Xu, A.B. Yu, Numerical simulation of the gas-solid flow in a fluidized bed by combining discrete particle method with computational fluid dynamics, Chem. Eng. Sci. 52 (1997) 2785–2809.

[14] Y. Tsuji, T. Kawaguchi, T. Tanaka, Discrete particle simulation of two-dimensional fluidized-bed, Powder Technol. 77 (1993) 79–87.

[15] J.A.M. Kuipers, K.J. Vanduin, F.P.H. Vanbeckum, W.P.M. Vanswaaij, Computer-simulation of the hydrodynamics of a 2-dimensional gas-fluidized bed, Comput. Chem. Eng. 17 (1993) 839–858.

[16] J.X. Bouillard, R.W. Lyczkowski, D. Gidaspow, Porosity distributions in a fluidized-bed with an immersed obstacle, AICHE J. 35 (1989) 908–922.

[17] C. Antoci, M. Gallati, S. Sibilla, Numerical simulation of fluid-structure interaction by SPH, Comput. Struct. 85 (2007) 879–890.

[18] M. Robinson, M. Ramaioli, S. Luding, Fluid-particle flow simulations using two-way-coupled mesoscale SPH-DEM and validation, Int. J. Multiphase Flow 59 (2014) 121–134.

[19] M.R. Hashemi, R. Fatehi, M.T. Manzari, SPH simulation of interacting solid bodies suspended in a shear flow of an Oldroyd-B fluid, J. Non-Newtonian Fluid Mech. 166 (2011) 1239–1252.

[20] D.G. Rong, T. Mikami, M. Horio, Particle and bubble movements around tubes immersed in fluidized beds – a numerical study, Chem. Eng. Sci. 54 (1999) 5737–5754.

[21] F.P. Di Maio, A. Di Renzo, D. Trevisan, Comparison of heat transfer models in DEM-CFD simulations of fluidized beds with an immersed probe, Powder Technol. 193 (2009) 257–265.

[22] C.L. Wu, J.M. Zhan, Y.S. Li, K.S. Lam, Dense particulate flow model on unstructured mesh, Chem. Eng. Sci. 61 (2006) 5726–5741.

[23] D.Y. Liu, C.S. Bu, X.P. Chen, Development and test of CFD-DEM model for complex geometry: a coupling algorithm for fluent and DEM, Comput. Chem. Eng. 58 (2013) 260–268.

[24] Y.Z. Zhao, M.Q. Jiang, Y.L. Liu, J.Y. Zheng, Particle-scale simulation of the flow and heat transfer behaviors in fluidized bed with immersed tube, AICHE J. 55 (2009) 3109–3124.

[25] Q.F. Hou, Z.Y. Zhou, A.B. Yu, Computational study of heat transfer in a bubbling fluidized bed with a horizontal tube, AICHE J. 58 (2012) 1422–1434.

[26] N. Gui, J.R. Fan, K. Luo, DEM-LES study of 3-D bubbling fluidized bed with immersed tubes, Chem. Eng. Sci. 63 (2008) 3654–3663.

[27] S.L. Yang, K. Luo, J.R. Fan, K.F. Cen, Particle-scale investigation of the hydrodynamics and tube erosion property in a three-dimensional (3-D) bubbling fluidized bed with immersed tubes, Ind. Eng. Chem. Res. 53 (2014) 6896–6912.

[28] F. Alobaid, J. Strohle, B. Epple, Extended CFD/DEM model for the simulation of circulating fluidized bed, Adv. Powder Technol. 24 (2013) 403–415.

[29] F. Alobaid, A particle-grid method for Euler-Lagrange approach, Powder Technol. 286 (2015) 342–360.

[30] C.S. Peskin, Flow Patterns around Heart Valves - Numerical Method, J. Comput. Phys. 10 (1972) 252–&.

[31] S. Takeuchi, S. Wang, M. Rhodes, Discrete element method simulation of three-dimensional conical-base spouted beds, Powder Technol. 184 (2008) 141–150.

[32] Y. Guo, C.Y. Wu, C. Thornton, Modeling gas-particle two-phase flows with complex and moving boundaries using DEM-CFD with an immersed boundary method, AICHE J. 59 (2013) 1075–1087.

[33] T. Tsuji, K. Higashida, Y. Okuyama, T. Tanaka, Fictitious particle method: a numerical model for flows including dense solids with large size difference, AICHE J. 60 (2014) 1606–1620.

[34] K. Higashida, K. Rai, W. Yoshimori, T. Ikegai, T. Tsuji, S. Harada, J. Oshitani, T. Tanaka, Dynamic vertical forces working on a large object floating in gas-fluidized bed: discrete particle simulation and Lagrangian measurement, Chem. Eng. Sci. 151 (2016) 105–115.

[35] Z.Y. Zhou, S.B. Kuang, K.W. Chu, A.B. Yu, Discrete particle simulation of particle-fluid flow: model formulations and their applicability, J. Fluid Mech. 661 (2010) 482–510.

[36] C.L. Wu, A.S. Berrouk, K. Nandakumar, Three-dimensional discrete particle model for gas-solid fluidized beds on unstructured mesh, Chem. Eng. J. 152 (2009) 514–529.

[37] C.L. Wu, K. Nandakumar, A.S. Berrouk, H. Kruggel-Emden, Enforcing mass conservation in DPM-CFD models of dense particulate flows, Chem. Eng. J. 174 (2011) 475–481.

[38] M. Afkhami, A. Hassanpour, M. Fairweather, D.O. Njobuenwu, Fully coupled LES-DEM of particle interaction and agglomeration in a turbulent channel flow, Comput. Chem. Eng. 78 (2015) 24–38.

[39] C.B. Fonte, J.A.A.O. Jr, L.C.D. Almeida, DEM-CFD coupling: mathematical modelling and case studies using Rokcy-DEM and ANSYS fluent, Eleventh International Conference on CFD in the Minerals and Process Industries, CSIRO, Melbourne, Australia, 7–9 December 2015, 2015.

[40] K.W. Chu, A.B. Yu, Numerical simulation of the gas-solid flow in three-dimensional pneumatic conveying bends, Ind. Eng. Chem. Res. 47 (2008) 7058–7071.

[41] K.W. Chu, A.B. Yu, Numerical and experimental investigation of an "S-shaped" circulating fluidized bed, Powder Technol. 254 (2014) 460–469.

[42] H. Wahyudi, K.W. Chu, A.B. Yu, 3D particle-scale modeling of gas-solids flow and heat transfer in fluidized beds with an immersed tube, Int. J. Heat Mass Transf. 97 (2016) 521–537.

[43] K.W. Chu, B. Wang, D.L. Xu, Y.X. Chen, A.B. Yu, CFD-DEM simulation of the gas-solid flow in a cyclone separator, Chem. Eng. Sci. 66 (2011) 834–847.

[44] K.W. Chu, B. Wang, A.B. Yu, A. Vince, CFD-DEM modelling of multiphase flow in dense medium cyclones, Powder Technol. 193 (2009) 235–247.

[45] T.B. Anderson, R. Jackson, A fluid mechanical description of fluidized beds, Ind. Eng. Chem. Fundam. 6 (1967) 527–&.

[46] Y.C. Zhou, B.D. Wright, R.Y. Yang, B.H. Xu, A.B. Yu, Rolling friction in the dynamic simulation of sandpile formation, Physica A 269 (1999) 536–553.

[47] R.D. Mindlin, H. Deresiewicz, Elastic spheres in contact under varying oblique forces, J Appl Mech-T Asme 20 (1953) 327–344.

[48] Y. He, Z. Wang, T.J. Evans, A.B. Yu, R.Y. Yang, DEM study of the mechanical strength of iron ore compacts, Int. J. Miner. Process. 142 (2015) 73–81.

[49] R. Beetstra, M.A. van der Hoef, J.A.M. Kuipers, Drag force of intermediate Reynolds number flow past mono- and bidisperse arrays of spheres, AICHE J. 53 (2007) 489–501.

[50] S. Ergun, Fluid flow through packed columns, Chem. Eng. Prog. 48 (1952) 89–94.

[51] C.Y. Wen, Y.H. Yu, Mechanics of fluidization, Chem. Eng. Prog. Symp. Ser. 62 (1966) 100–111.

[52] C.R. Muller, S.A. Scott, D.J. Holland, B.C. Clarke, A.J. Sederman, J.S. Dennis, L.F. Gladden, Validation of a discrete element model using magnetic resonance measurements, Particuology 7 (2009) 297–306.

[53] C.R. Muller, D.J. Holland, A.J. Sederman, S.A. Scott, J.S. Dennis, L.F. Gladden, Granular temperature: comparison of magnetic resonance measurements with discrete element model simulations, Powder Technol. 184 (2008) 241–253.

[54] W.G. Nan, Y.S. Wang, J.Z. Wang, Numerical analysis on the fluidization dynamics of rodlike particles, Adv. Powder Technol. 27 (2016) 2265–2276.

[55] T.W. Li, R. Garg, J. Galvin, S. Pannala, Open-source MFIX-DEM software for gas-solids flows: part II - validation studies, Powder Technol. 220 (2012) 138–150.

[56] G.A. Bokkers, M.V.S. Annaland, J.A.M. Kuipers, Mixing and segregation in a bidisperse gas-solid fluidised bed: a numerical and experimental study, Powder Technol. 140 (2004) 176–186.

[57] J.A. Doherty, R.S. Verma, S. Shrivastava, S.C. Saxena, Heat-transfer from immersed horizontal tubes of different diameter in a gas-fluidized bed, Energy 11 (1986) 773–783.

[58] J. Friedman, P. Koundakjian, D. Naylor, D. Rosero, Heat transfer to small horizontal cylinders immersed in a fluidized bed, J Heat Trans-T Asme 128 (2006) 984–989.

[59] D.H. Glass, D. Harrison, Flow patterns near a solid obstacle in a fluidized bed, Chem. Eng. Sci. 19 (1964) 1001–&.